Preparation of a novel anti-aggregation silica/zinc/graphene oxide nano-composite with enhanced adsorption capacity

Yajun Yue[a,b], Zhanfang Cao*[a], Fan Yang[a], Jing Wang[a], Isaac Abrahams*[b]

* Corresponding authors

E-mail addresses: zfcao@mail.csu.edu.cn, i.abrahams@qmul.ac.uk

a: College of Chemistry and Chemical Engineering, Central South University, Changsha 410083, China

b: Materials Research Institute, School of Biological and Chemical Sciences, Queen Mary University of London, London, E1 4NS, United Kingdom

Graphical Abstract
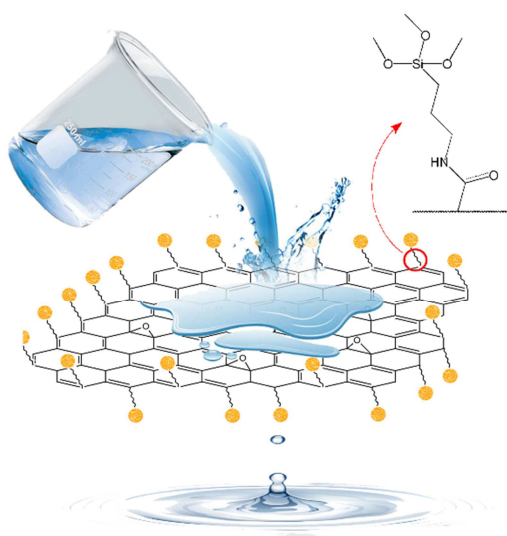
A nano-silica/zinc/graphene oxide composite (GO-NMSZ) has been prepared with good adsorption capacity and filtration efficiency. The rich number of active metal sites as well as the high oxidation level of the GO sheets result in a multi-effect mechanism, involving non-selective chemical and physical adsorption. These characteristics make it applicable in dye-wastewater purification.

Abstract

Nanomaterials play a significant role in adsorption treatment of dye wastewater, however, irreversible aggregation of nanoparticles poses a significant problem. In this work, nano-mesoporous zinc doped silicate (NMSZ) was prepared through an *in situ* method. To prevent agglomeration, NMSZ was covalently bonded to graphene oxide (GO) sheets to form a nano-silica/zinc/graphene oxide composite (GO-NMSZ), targeted at cationic methylene blue (MB) removal. For comparison, undoped mesoporous silica (MS) was also synthesized and modified to obtain a silica/graphene/oxide composite (GO-MS). Materials were characterized by X-ray powder diffraction (XRD), scanning electron microscopy (SEM), Fourier transform infrared (FT-IR) spectroscopy, transmission electron microscopy (TEM), nitrogen sorption and X-ray photoelectron spectroscopy (XPS). The oxygen containing groups of GO were preserved in the composites leading to higher adsorption capacities. The best GO-NMSZ composite exhibited an enhanced adsorption capacity of 100.4 mg·g^{-1} for MB compared to that of undoped GO-MS (80.1 mg·g^{-1}) and non-grafted NMSZ (55.7 mg·g^{-1}). The non-selective character of GO-NMSZ is demonstrated by effective adsorption of anionic Congo red (127.4 mg·g^{-1}) and neutral isatin (289.0 mg·g^{-1}). The adsorption kinetics, adsorption isotherms and a thermodynamic study suggest MB adsorption occurs through chemisorption and is endothermic in nature.

Key words: Dye adsorption, graphene oxide, nanocomposite, water purification

1. Introduction

Safe drinking water is vital to all higher life forms. Nevertheless, around 780 million people still lack adequate clean water.[1] Industrial pollutants such as organic dyes increase the cost and difficulty of providing access to safe water.[2] Moreover, dyes are typically chemically stable and can be carcinogenic and mutagenic.[3] Methylene blue (MB) is a common sulfur containing dye that has been linked to heart disease and high concentrations can lead to increased heart rate, vomiting, shock, cyanosis, jaundice and even quadriplegia.[4]

Techniques such as membrane separation,[5] photocatalytic degradation,[3b] electrochemical oxidation[6] and adsorption methods[7] have been reported to purify polluted water, amongst which the most cost-effective method is adsorption due to its low cost and convenient operation. Much work so far has focused on developing highly efficient adsorbents.

Mesoporous silicas are a promising option and they have attracted much attention due to their adjustable pore diameter and large surface area. However, physisorption in pure mesoporous silica (MS) is relatively inefficient. Therefore, doping with metallic elements e.g. Al, Ti, Zn, V, Fe and Cu is often performed to increase the number of active sites.[8] Among these elements, zinc has excellent affinity for sulfur and can thus be used for the removal of sulfur-containing compounds. The adsorption mechanism for MB removal using zinc doped silicate is proposed to be chemisorption, based on a Zn-S coordinate bond, resulting in enhanced interaction between adsorbent and pollutant.[9]

Another high-performance material, graphene oxide (GO), has large surface area, due to its sheet-like structure, which includes numerous oxygen-containing functional groups, e.g. hydroxy(-OH), carboxyl (-COOH) and epoxy (C-O-C). These functional groups exhibit negative charges in solution and therefore can attract metallic cations and cationic groups.[10] The sheet-like structure of GO, combined with its high electronic conductivity result in exceptionally high adsorption capacity for this material, but interaction between sheets can cause

irreversible aggregation. Although there have been remarkable reports concerning GO as an adsorbent, the material is highly soluble and the most problematic step remains separation of the GO sheets from solution. This means reuse of GO sheets is practically challenging. Meanwhile, the nano-scale mesoporous material is also easily stuck in the process of filtration. One approach to solving this problem is to attach magnetic particles, which can then be attracted to an external magnet. Yao *et al.*[11] deposited Fe_3O_4 onto GO sheets using a reduction method, but found that the maximum adsorption capacity for MB was only 45.27 mg·g^{-1}. Wang *et al.*[12] synthesized a magnetic composite composed of GO, carbon nanotubes (CNT) and Fe_3O_4 nanoparticles for MB adsorption and obtained a higher maximum adsorption capacity of 65.79 mg·g^{-1}. The main problem with this method is reduction of the oxygen containing groups on the GO surface, which results in decreased adsorption capacity.

In order to solve the aforementioned problems, in the present work we have designed and synthesized a novel nanocomposite by chemically binding GO sheets with zinc doped mesoporous silica. The structure and morphology of these materials was investigated by X-ray powder diffraction, electron microscopy and FTIR spectroscopy. The developed nanocomposite shows enhanced adsorption capacity for MB.

2. Experimental

2.1. Materials

Starting materials used in this work were ethyl silicate (TEOS, AR), zinc chloride (AR), ammonium hydroxide (25 wt%), sulfuric acid (98 wt%), hexadecyltrimethyl ammonium bromide (CTAB, AR), ethyl alcohol absolute (AR), (3-aminopropyl)triethoxysilane (APTES) and methylbenzene, all purchased from Sinopharm Chemical Reagent Co., China. Graphite powder, N-N'-dicyclohexylcarbodiimide (DCC), dimethylformamide (DMF) and syringe filters (pore size of 0.45 μm) were purchased from Aladdin Industrial Corporation

(Shanghai, China).

2.2. Synthesis of materials

2.2.1. Preparation of MS, NMSZ and GO

CTAB (2.74 g) was dissolved in ethanol (50 ml) with vigorous stirring. To this solution TEOS (5 ml) was added dropwise, followed by addition of distilled water (100 ml). Concentrated ammonium hydroxide was used to adjust the solution pH to 10. After four hours of stirring, the obtained white gel was washed three times with ethanol and distilled water. After drying in an oven at 105 °C for 8 h, the sample was calcined in a muffle furnace at 500 °C for 3 h (heating rate: 2 °C min^{-1}) to obtain the MS. For NMSZ, zinc chloride (0.30 g) was slowly added to the CTAB/TEOS solution before the addition of ammonium hydroxide. The rest of the procedure was identical.

Graphene oxide was prepared using a modification of the Hummers method.[13] Under stirring, H_2SO_4 (23 ml, 98 wt%), graphite powder (1 g) and $NaNO_3$ powder (0.5 g) were added successively to a flask in an ice bath (4 °C), followed by the addition of $KMnO_4$ powder (3 g). After 1 h of reaction, the flask was transferred to a water bath at 35 °C for another 0.5 h. Then, 80 ml of distilled water were added and the temperature was kept between 70-100 °C for 0.5 h. This was followed by the addition of 60 ml distilled water and 15 ml (30 wt%) hydrogen peroxide. After reaction for 15 min, 4 ml hydrochloric acid (30 wt%) were added. When the color of the solution became golden, centrifugation (7500 rpm, 10 min) was performed to separate solid and liquid phases. The solid sample was washed with distilled water until the washings were neutral and then dried in a vacuum tank at 40 °C.

2.2.2. Preparation of GO-MS and GO-NMSZ

To functionalize the mesoporous silicas, 1 g of MS or NMSZ powder was boiled in distilled water for 3 h to activate the surface hydroxyl groups. The powders were then filtered and dried at 60 °C for 2 h. The dried powders were then dispersed in 100 ml methylbenzene, to which 6 ml of APTES were added and the solution heated under

reflux at 120 °C for 24 h. The solids were filtered, washed once with ethanol and dried in a vacuum drying oven at 60 °C. The functionalized MS and NMSZ powders were anchored to GO using a post-grafting method. 0.04 g of GO was dispersed in 100 ml DMF solution under ultrasonic treatment for 30 min. To this dispersion, 0.05 g of DCC and different amount of the functionalized powders were added. The mass ratios of NMSZ to GO used were 20:1, 10:1, 5:1, 2:1, 1:5 and 1:20. The reaction was heated at 80 °C for 24 h and the obtained solids were filtered, washed with toluene and dried at 50 °C in a vacuum oven. The reaction scheme is summarized in Fig. 1.

2.3. Characterization

X-ray powder diffraction (XRD) patterns were obtained on a Siemens D500 diffractometer (Germany) with Cu-Kα radiation (λ = 1.5418 Å). Morphology was determined by scanning electron microscopy (SEM) using a field emission scanning electron microscope (Nova Nano SEM 230, FEI Electron Optics B.V., Czech Republic). TEM images were recorded on a Tecnai G2 F20 S-TWIN TMP (FEI Co. Ltd, Czech Republic) at 200 kV. Infrared spectroscopy was carried out on a Nicolet 6700 IR spectrometer (Thermo Electron Scientific Instruments, U.S.A) over the wavenumber range 400 to 3000 cm^{-1}. X-ray photoelectron spectra (XPS) were recorded in constant analyzer energy (CAE) mode (Escalab 250Xi, Thermo Fisher Scientific, U.S.A), with binding energy measured with reference to the C 1s peak at 284.8 eV. Nitrogen adsorption/desorption isotherms were determined on a Kubo X1000 porosimeter (Builder Co. Ltd., Beijing). All samples were dried at 150 °C for > 4 hours before measurements. Total surface area was measured using the Brunauer-Emmet-Teller (BET) method. The total pore volume (V_t) was calculated at a relative pressure p/p$_0$ of 0.99 and the pore size distributions were analyzed by the Barrett-Joyner-Halenda (BJH) method.

2.4. Adsorption experiments

20 mg of each absorbent was mixed with 20 ml dye solution in a conical flask,

and then shaken until reaching equilibrium (ca. 20 h) on an oscillator. The filtrate was collected with record of filtration time (t) and then diluted to an appropriate concentration. The quantity adsorbed q_e (in mg·g^{-1}) was calculated using equation (1):

$$q_e = \frac{(C_0 - C_e)V}{m} \times 100\% \tag{1}$$

where m (g) is the absorbent mass, and V (L) is the total volume of test solution. C_0 (mg·L^{-1}) and C_e (mg·L^{-1}) represent the initial and equilibrium concentrations, respectively. Experiments were carried out in triplicate.

3. Results and discussion

3.1. Sample characterization

Fig. 2a shows the small-angle XRD patterns of MS and NMSZ. Three peaks are evident in the diffraction pattern for MS at 2.43°, 4.10° and 4.71° 2θ, corresponding to the (100), (110) and (200) peaks of the hexagonal structure of MCM-41,[14] confirming that an ordered mesoporous microstructure was formed. d_{100} was confirmed as 3.63 nm. After doping with zinc, the (100) peak broadens significantly and shifts to lower angle. The (110) and (200) peaks are not evident in the pattern of the zinc doped sample, indicating that zinc doping results in amorphization. A possible reason for this is the strain caused by the larger ionic radius of zinc (0.60 Å) compared to that of silicon (0.26 Å).[15] Another factor that could cause this amorphization is the fact that zinc cations could preferentially attract silicate groups during gelation, forming sol-gel precursors with much smaller size. Fig. 2b shows the conventional XRD patterns of NMSZ and GO-NMSZ. There is an absence of sharp Bragg peaks in the pattern of NMSZ, with only a broad halo centered at around 24° 2θ, confirming its amorphous character. In contrast, the pattern for GO-NMSZ shows not only the amorphous halo due to NMSZ, but also a sharp intense peak at 10.5° 2θ attributed to the (002) plane of GO,[16] corresponding to an interlayer distance of 8.43 Å, confirming preservation of the layer structure. It has been reported that the peak at

10.5° 2θ shifts to around 26.1° indicating a decreased interlayer spacing as a result of the reduction of GO,[10, 17] which often happens when modified with Fe_3O_4 particles.[18] The results of the present study suggest preservation of the oxygen containing groups in the composites. Oxygen containing groups like –OH, C=O, C-O and C-OH are of great significance for adsorption of MB and therefore the conservation of these groups in the composites is likely to be beneficial for MB removal.[19]

Fig.3 shows representative SEM and TEM images of the studied samples. The MS sample (Fig. 3a) was found to exhibit regular spherical shaped particles, with an average diameter of 358 nm. Zinc doping (Fig. 3b) results in much smaller particles of around 105 nm in size. Particles of NMSZ exhibit significantly greater agglomeration than seen in MS, due to the greatly increased surface energy, as reported previously.[20] Despite the relatively high surface area, this agglomeration reduces the number of sites available for adsorption and hence decreases the adsorption capacity. Fig. 3c and Fig. 3d show the morphology of GO-MS and GO-NMSZ, respectively. It can be seen that GO sheets remain intact, with silica particles located near the sheet edges, consistent with the carboxyl groups, on the sheet edges, acting as the reactive groups during grafting. This effect is more evident in the GO-NMSZ sample, as smaller particles of NMSZ have greater surface area and hence higher reactivity than undoped MS. Furthermore, the presence of these particles at the edges limits agglomeration of the GO sheets, a particular problem with GO.

TEM images of MS (Fig. 3e) confirm a regular spherical shape with internal pore structures. These worm-like pores are irregular and interconnected, contributing to a large surface area. Fig. 3f reveals that NMSZ retains the multi-pore structure, but with much smaller particle sizes. This may be due to the zinc cations preferentially attracting silicate ions and reducing the repulsion of the latter. The formed precursors come together though a self-assembly process, according to the liquid crystal templating (LCT) mechanism.[21] Particles are found to be wrapped in GO sheets after grafting (Fig. 3g and 3h). The insertion of particles between the thin GO sheets,

effectively prevents the agglomeration of both the GO sheets and the nanoparticles.

Fig. 4a shows the FT-IR spectra of as prepared GO and MS samples compared to that of a sample of MS after treatment with APTES (NH$_2$-MS) and after grafting to GO (GO-MS). In the spectrum of GO, the peak located at 1726 cm^{-1} corresponds to C=O vibration, while that at 1224 cm^{-1} is attributed to C-OH groups. Peaks centered at 1050 cm^{-1}, 1620 cm^{-1} and 3410 cm^{-1} result from C-O, C=C and -OH groups respectively, suggesting the graphene was well oxidized.[22] In the spectrum of MS, the peaks located at 1102 cm^{-1}, 810 cm^{-1} and 470 cm^{-1} correspond to the asymmetrical stretching, symmetrical stretching and bending vibrations of Si-O-Si, while that at 964 cm^{-1} is associated with the stretching vibration of Si-O-(H…H$_2$O) and its disappearance after amination suggests the consumption of Si-OH groups. The peak at 1637 cm^{-1} is attributed to the H-O-H bending vibration of water adsorbed onto the surface.[23] After modification, peaks appear at 2938 cm^{-1} and 2870 cm^{-1} in both NH$_2$-MS and GO-MS and are due to the asymmetrical stretching and stretching vibrations of C-H, respectively. The peaks at 1567 cm^{-1} and 1500 cm^{-1} in NH$_2$-MS can be attributed to primary amine bending, while that at 694 cm^{-1} is associated with the N-H bending vibration. The decreased intensity of the peak at 3410 cm^{-1}, associated with surface -OH groups, is consistent with condensation of Si-OH groups to form Si-O-Si linkages. On grafting MS to GO, the vibrations at 1650 cm^{-1} of GO-MS are associated with secondary amide stretching vibrations.[24] Fig. 4b shows FTIR spectra of NMSZ, NH$_2$-NMSZ and GO-NMSZ. Being similar to MS, the bands at 1080 cm^{-1} and 795 cm^{-1} are associated with the Si-O-Si asymmetrical stretching and stretching vibrations, respectively. As the amount of added zinc was relatively very small, peaks due to Zn-O vibrations could not be observed. After modification, the primary amine stretching vibration peaks appeared at 1560 cm^{-1} and 1500 cm^{-1} and those associated with secondary amide and C=O groups are found at 1650 cm^{-1} and 1390 cm^{-1}.[10]

Fig. 5 shows the nitrogen adsorption/desorption isotherms and pore size distribution parameters of as-synthesized MS, NMSZ, GO-MS and GO-NMSZ. The isotherms correspond to type IV, indicating the existence of numerous micro-pores.

No hysteresis loop was observed, suggesting that capillary condensation was unlikely, due to the relatively small pore size. The BJH method gave an average pore size of 3.85 nm for MS, which is quite consistent with the d_{100} value (calculated as 3.64 nm), while the doping produced contraction of pore structure and resulted in a smaller average pore size of 2.02 nm. NMSZ shows a higher BET surface area (451.16 $m^2 \cdot g^{-1}$) than MS (305.87 $m^2 \cdot g^{-1}$) because of the smaller particle size. However, the grafting of GO sheets reduces the surface area significantly due to the strong interaction. The evident overlap of particles and layers, which can be observed in the TEM images, is responsible for the sharp decrease in pore distribution.

Fig. 6a depicts the XPS full-scan spectra of GO-NMSZ before and after adsorption, with the magnified S $2p$ peak indicating successful adsorption. Detailed scans of the S and Zn spectra are shown in Fig. 6b-d. The S $2p$ spectrum shows characteristic $2p_{3/2}$ and $2p_{1/2}$ peaks with binding energies of 164.12 eV and 165.35 eV, respectively, which are slightly lower than the previously reported values for S atoms in MB a 164.63 eV and 165.81 eV, respectively,[9] reflecting the interaction between the dye molecule and GO sheets. The fitted Zn $2p_{3/2}$ spectrum indicates there are at least three zinc species and one of them is dominant. The peak at 1022.2 eV before adsorption is consistent with the presence of Zn-O species.[25] The less intense peak at 1021.2 eV could be associated with metallic Zn atoms[26] and after adsorption this peak diminishes as the metallic zinc oxidizes. The higher binding energy peak at 1024.1 eV prior to adsorption lies above the range for Zn-O-Si type species whose binding energies are generally below 1023 eV[27] and is tentatively assigned to zinc bonded to strong electrophilic groups such as the oxygen containing groups on GO sheets. After adsorption, there is a negative shift in the binding energies of all three species. The low binding energy peak attributed to metallic zinc almost disappears. The shift to lower binding energies is attributed to the formation of Zn-S coordinate bonds. The formation of these bonds could account for the higher adsorption capacity of NMSZ compared to MS. Thus it is proposed that the mechanism of MB adsorption, likely involves electrostatic interaction deriving from the GO component and

chemisorption due to the metallic sites.[28]

3.2. Adsorption experiments

Fig. 7 shows the mass ratio dependence of adsorption capacity and filtration rate. The equilibrium adsorption capacity generally increases when the ratio of GO increases, while at the same time, the filtration rate drops quickly. The optimized ratio of NMSZ:GO is determined to be 5:1, as this composition exhibits the highest filtration rate with reasonable adsorption capacity. Fig. 8 shows the adsorption capacity of MB onto samples prepared by different methods. The MB uptake onto MS and NMSZ was determined to be 24.4 mg·g^{-1} and 55.7 mg·g^{-1}, respectively. Similar effects were also found in other meso porous silica materials doped with Ti, Al and Ag.[29] After being grafted onto GO, the adsorption capacity increased remarkably to 100.37 mg·g^{-1}, which suggests that a synergistic effect between GO and NMSZ promotes the adsorption capacity, while the adsorption by GO-MS was much weaker under the same conditions. In comparison to the cationic dye, two other dyes, Congo red (anionic dye) and isatin (neutral dye), whose adsorption mechanisms are likely to involve π-π interactions, were also tested to investigate the selectivity of GO-NMSZ. Large adsorption capacities of up to 127 mg·g^{-1} and 289 mg·g^{-1} were observed for Congo red and isatin, respectively, suggesting that the adsorption of GO-NMSZ is non-selective. As it showed the largest adsorption capacity, the adsorption behavior of GO-NMSZ with a mass ratio of 5:1 was further investigated. Table 1 lists the adsorption capacities of the materials in the present work compared to those of other reported composite materials coupled with graphene or GO. The agglomeration effect and lack of active sites in these materials are responsible for their relatively low adsorption capacity.

Table 1 Comparison of adsorption capacities of composites based on graphene and graphene oxide

Adsorbents	MB uptake (mg·g^{-1})	Ref.
Magnetic Fe$_3$O$_4$@graphene	45.27	[11]
Magnetic graphene-carbon nanotube	65.79	[12]
Magnetic Cellulose/Graphene	52.5	[30]
Zinc ferrite–reduced graphene oxide	9.55	[31]
Graphene oxide–poly(2-hydroxyethyl methacrylate)	39.41	[32]
Polyvinyl alcohol/graphene oxide hydrogels	59.56	[33]
Hydroxypropyl cellulose/graphene oxide	27.85	[34]
Modified magnetic graphene oxide	76.35	[35]
MS	24.4	*This work*
NMSZ	55.7	*This work*
GO-MS	80.14	*This work*
GO-NMSZ	100.37	*This work*

Analysis of adsorption kinetics was carried out by fitting three kinetic models viz.: the pseudo-first-order, the pseudo-second-order and Webber-Morris models. The corresponding equations are given as equations 2, 3 and 4, respectively.

$$\ln(q_e - q_t) = \ln q_e - k_1 t \tag{2}$$

$$\frac{t}{q_t} = \frac{1}{k_2 q_e^2} + \frac{t}{q_e} \tag{3}$$

$$q_t = k_{id} t^{0.5} + C \tag{4}$$

where the k_1 is the first-order rate constant (min^{-1}), t is the contact time (min), q_e and q_t are the adsorption capacity (mg·g^{-1}) at equilibrium and at time t, respectively, k_2 is the second-order rate constant (g·mg^{-1}·min^{-1}), k_{id} is the inter-particle diffusion rate (mg·g^{-1}·min^{-1}) and C is a coefficient related to the interface layer (mg·g^{-1}).

Fitting with the pseudo-first-order model, as shown in Fig. 9a, was unsatisfactory. This model is based on a diffusion-control mechanism, with a heavy dependence on

the constant concentration of absorbates, and thus the model deviates with decreasing dye concentration.[36] The pseudo-second-order model was more effective in describing the adsorption process, as shown in Fig. 9b and assumes that the reconstructed adsorption kinetics are correlated with the number of vacant active sites in the chemisorption process.[37] This is consistent with our previous work.[9] Fig. 9c shows fits using the Webber-Morris model. This model provides information on intra-particle diffusion and assumes three steps: adsorbate molecules firstly spread across the boundary layer that surrounds the particles; they then transfer into the internal structure through surface and branched pores and are finally trapped by adsorbent sites.[38] The three stages of adsorption are evident with the fastest adsorption rate in the first stage, due to the high driving forces. The relevant parameters are listed in Table 2.

Table 2 Adsorption kinetics parameters for MB adsorption onto GO-NMSZ

T (°C)	Pseudo-first-order				Pseudo-second-order		
	q_e(mg·g^{-1})	q_e (mg·g^{-1})	$k_1 \times 10^{-3}$ (min^{-1})	R^2	q_e (mg·g^{-1})	$k_2 \times 10^{-4}$(g·mg^{-1}·min^{-1})	R^2
25	97.66	84.32	2.7	0.8508	106.38	0.5156	0.9768
35	101.99	61.52	3.3	0.9107	107.52	1.4015	0.9973
45	119.30	62.87	4.0	0.9589	123.46	1.7256	0.9985

T (°C)	Webber-Morris					
	K_{id} (mg·g^{-1}· min$^{0.5}$)	R^2	K_{id} (mg·g^{-1}· min$^{0.5}$)	R^2	K_{id} (mg·g^{-1}· min$^{0.5}$)	R^2
25	6.1679	0.9935	2.2092	0.9167	0.3722	0.9615
35	5.9877	0.9599	0.7342	0.9751	0.4205	0.7376
45	6.1663	0.9428	1.6898	0.8643	0.2386	0.8355

The adsorption mechanisms were investigated by Langmuir, Freundlich and Dubinin-Radushkevich isotherms with the results shown in Fig. 10 and Table 3.

(1) Langmuir isotherm

The Langmuir isotherm is an idealized model for description of chemisorption processes. It assumes adsorption on the surface of the adsorbent is homogeneous and induced by a monolayer without interaction effects between adsorbates. The linearized equation is given as follows:

$$\frac{C_e}{q_e} = \frac{1}{q_0 K_L} + \frac{C_e}{q_0} \tag{5}$$

where C_e (mg·L^{-1}) is the equilibrium concentration, K_L (L·mg^{-1}) is the adsorption equilibrium constant and q_0 (mg·g^{-1}) is the maximum adsorption quantity. The favorability of adsorption can be expressed by factor R_L in equation (6):

$$R_L = \frac{1}{1 + K_L C_0} \tag{6}$$

where C_0 (mg·L^{-1}) is the initial concentration of adsorbates. The adsorption process is known to be favorable if $0 < R_L < 1$, unfavorable if $R_L > 1$ and irreversible if $R_L = 0$.

(2) Freundlich isotherm

The Freundlich isotherm gives a reliable description of heterogeneous adsorption processes and is given by equation (7):

$$\ln q_e = \ln K_F + \frac{1}{n} \ln C_e \tag{7}$$

where K_F (mg·g^{-1})(L·g^{-1})^n is the adsorption equilibrium constant and n is the inhomogeneity coefficient.

(3) Dubinin–Radushkevich (D-R) isotherm

The D-R isotherm can be used to identify physisorption and chemisorption and is described by:

$$\ln q_e = \ln q_m - \beta [RT \ln(1 + \frac{1}{C_e})]^2 \tag{8}$$

$$E = (2\beta)^{-0.5} \tag{9}$$

where the q_m (mg·g^{-1}) is the D-R isotherm constant, β (mol^2·kJ^2) is the activity coefficient related to average adsorption energy, R is the gas constant (8.314 J·mol^{-1}·K^{-1}), T (K) is temperature in Kevin and E (kJ·mol^{-1}) is the free energy. Adsorption can be attributed to physisorption ($E < 8$ kJ·mol^{-1}), ion exchange (8 kJ·mol^{-1} < E < 16.2 kJ·mol^{-1}) and strong chemisorption ($E > 20$ kJ·mol^{-1}).

Table 3 Adsorption isotherm parameters for MB adsorption onto GO-NMSZ

$T(°C)$	Langmuir				Freundlich			Dubinin-Radushkevich		
	$K_L(\text{L·mg}^{-1})$	$q_0(\text{mg·g}^{-1})$	R^2	R_L	$K_F(\text{mg·g}^{-1})(\text{L·g}^{-1})^n$	$1/n$	R^2	q_m	E (kJ·mol^{-1})	R^2
25	0.00592	158.98	0.9876	0.25~0.63	12.08	0.4172	0.8710	124.26	40.25	0.9689
35	0.01026	194.93	0.9894	0.16~0.49	11.53	0.4517	0.9409	137.65	42.47	0.9102
45	0.01523	207.90	0.9886	0.12~0.40	15.67	0.4316	0.8829	161.15	50.68	0.9515

The adsorption was found to be best fitted with the Langmuir model in comparison to the Freundlich and Dubinin-Radushkevich models. An increase in adsorption capacity at higher temperatures was observed, which can be attributed to the reduced viscosity of the solution and the faster molecular motion, being consistent with an endothermic process, as discussed in previous research.[39] The coefficients (0 < R_L < 1) suggest the adsorption of MB onto GO-NMSZ was favorable at room temperature. The Dubinin-Radushkevich model also gave a reasonable R^2 coefficient and a free adsorption energy of more than 40 kJ·mol^{-1} and reflects that the adsorption was chemically driven.

Thermodynamic parameters were calculated using the Van't Hoff equation:

$$\ln(\frac{q_e}{C_e}) = -\frac{\Delta H}{RT} + \frac{\Delta S}{R} \tag{10}$$

$$\Delta G = \Delta H - T\Delta S \tag{11}$$

where ΔH (kJ·mol^{-1}) represents enthalpy change, ΔS (J·mol^{-1}·K^{-1}) is the entropy change and ΔG (kJ·mol^{-1}) is the Gibbs free energy change.

Equation (12) can be used to estimate the activation energy:

$$\ln k_2 = \ln A - \frac{E_a}{RT} \tag{12}$$

where k_2 (g·mol^{-1}·s^{-1}) is the rate constant of the pseudo-second-order model, A (g·mol^{-1}·s^{-1}) is the Arrhenius factor, which is independent of temperature and E_a (kJ·mol^{-1}) is the activation energy.

The thermodynamic parameters were calculated for different initial concentrations of MB solution ranging from 100 mg·L^{-1} to 500 mg·L^{-1} and the results are displayed in Fig. 11. The positive change of enthalpy is consistent with the results

of the isotherm analysis, suggesting that MB adsorption onto GO-NMSZ is an endothermic process. The spontaneous adsorption process is evidenced by the negative values of ΔG. It is worth mentioning that for the same initial MB concentration, ΔG values reduce significantly with increasing temperature, meaning the adsorption is accelerated by higher temperatures. The decrease in the absolute value of ΔG with increasing initial MB concentration (at a particular temperature) is due to the decreased equilibrium constant, resulting in weaker adsorption efficiency. The plot of ln k_2 versus $1/T$ is linear (Fig. 11b) and the activation energy was determined to be 37.29 kJ·mol^{-1}, suggesting a chemisorption process for adsorption of MB onto GO-NMSZ.

4. Conclusions

In this paper, a new series of adsorbents was successfully synthesized and tested for dye removal. Compared to pure mesoporous silica, doping with zinc is found to improve the adsorption capacity for MB from 24.4 mg·g^{-1} to 55.7 mg·g^{-1} due to the increased number of active sites. Particle sizes were also noticeably reduced to the nanoscale after doping, with a contraction of pore size. Chemical modification by binding particles with GO sheets was successfully carried out using a post-grafting method and affords a significant improvement of the adsorption capacity to 100.37 mg·g^{-1}. The kinetics of MB adsorption suggest a mechanism involving chemisorption. MB adsorption is found to be a spontaneous endothermic process. As well as the cationic dye MB, GO-NMSZ exhibits significant adsorption capacities for the anionic and neutral dyes, Congo red and isatin, respectively, confirming GO-NMSZ is non-selective and indicating its potential for adsorption of a range of pollutants.

References

[1] W. P. Schmidt, *Tropical Medicine & International Health* **2014**, *19*, 522-527.

[2] M. Hemmati, A. Asghari, M. Ghaedi, M. Rajabi, *Journal of the Taiwan Institute of Chemical Engineers* **2017**.

[3] a) M. Wawrzkiewicz, M. Wiśniewska, V. M. Gun'ko, V. I. Zarko, *Powder Technology* **2015**, *278*, 306-315; b) M. Tian, C. Dong, X. Cui, Z. Dong, *Rsc Advances* **2016**, *6*.

[4] a) M. T. Uddin, M. A. Islam, S. Mahmud, M. Rukanuzzaman, *Journal of Hazardous Materials* **2009**, *164*, 53-60; b) A. Asfaram, M. Ghaedi, M. A. Azqhandi, A. Goudarzi, M. Dastkhoon, *RSC Advances* **2016**, *6*, 40502-40516.

[5] M. Liu, Q. Chen, K. Lu, W. Huang, Z. Lü, C. Zhou, S. Yu, C. Gao, *Separation & Purification Technology* **2017**, *173*, 135-143.

[6] M. Zhou, J. He, *Electrochimica Acta* **2007**, *53*, 1902-1910.

[7] M. T. Yagub, T. K. Sen, S. Afroze, H. M. Ang, *Advances in Colloid and Interface Science* **2014**, *209*, 172-184.

[8] a) K. Ahmed, F. Rehman, C. T. Pires, A. Rahim, A. L. Santos, C. Airoldi, *Microporous and Mesoporous Materials* **2016**, *236*, 167-175; b) B. Jeong, D. H. Kim, E. J. Park, M.-G. Jeong, K.-D. Kim, H. O. Seo, Y. D. Kim, S. Uhm, *Applied Surface Science* **2014**, *307*, 468-474; c) T.-D. Nguyen-Phan, E. W. Shin, V. H. Pham, H. Kweon, S. Kim, E. J. Kim, J. S. Chung, *Journal of Materials Chemistry* **2012**, *22*, 20504-20511; d) F. Yang, S. Gao, C. Xiong, S. Long, X. Li, T. Xi, Y. Kong, *RSC Advances* **2015**, *5*, 72099-72106; e) X. Li, Y. Kong, S. Zhou, B. Wang, *Journal of Materials Science* **2017**, *52*, 1432-1445; f) S. Kuai, Z. Nan, *Chemical Engineering Journal* **2014**, *244*, 273-281.

[9] Z. Cao, Y. Yue, H. Zhong, P. Qiu, P. Chen, X. Wen, S. Wang, G. Liu, *Journal of the Taiwan Institute of Chemical Engineers* **2017**, *71*, 464-473.

[10] X. Li, Z. Wang, Q. Li, J. Ma, M. Zhu, *Chemical Engineering Journal* **2015**, *273*, 630-637.

[11] Y. Yao, S. Miao, S. Liu, L. P. Ma, H. Sun, S. Wang, *Chemical Engineering Journal* **2012**, *184*, 326-332.

[12] P. Wang, M. Cao, C. Wang, Y. Ao, J. Hou, J. Qian, *Applied Surface Science* **2014**, *290*, 116-124.

[13] a) W. S. Hummers Jr, R. E. Offeman, *Journal of the American Chemical Society* **1958**, *80*, 1339-1339; b) C. Xu, J. Sun, L. Gao, *Journal of Materials Chemistry* **2011**, *21*, 11253-11258.

[14] C. Kresge, M. Leonowicz, W. J. Roth, J. Vartuli, J. Beck, *Nature* **1992**, *359*, 710.

[15] R. D. Shannon, *Acta crystallographica section A: Crystal Physics, Diffraction, Theoretical and General Crystallography* **1976**, *32*, 751-767.

[16] T. Nakajima, A. Mabuchi, R. Hagiwara, *Carbon* **1988**, *26*, 357-361.

[17] a) H. Wang, X. Yuan, Y. Wu, X. Chen, L. Leng, H. Wang, H. Li, G. Zeng, *Chemical Engineering Journal* **2015**, *262*, 597-606; b) E. Ma, J. Li, N. Zhao, E. Liu, C. He, C. Shi, *Materials Letters* **2013**, *91*, 209-212.

[18] a) H. Teymourian, A. Salimi, S. Khezrian, *Biosensors and Bioelectronics* **2013**, *49*, 1-8; b) V. Chandra, J. Park, Y. Chun, J. W. Lee, I.-C. Hwang, K. S. Kim, *ACS Nano* **2010**, *4*, 3979-3986.

[19] B. Hameed, A. Ahmad, *Journal of Hazardous Materials* **2009**, *164*, 870-875.

[20] a) M. Meng, Z. Gan, J. Zhang, K. Liu, L. Wang, S. Li, Y. Yao, Y. Zhu, J. Li, *Physica Status Solidi (b)* **2017**; b) J. Li, Y. Lin, B. Zhao, *Journal of Nanoparticle Research* **2002**, *4*, 345-349.

[21] a) J. Beck, J. Vartuli, W. J. Roth, M. Leonowicz, C. Kresge, K. Schmitt, C. Chu, D. H. Olson, E. Sheppard, S. McCullen, *Journal of the American Chemical Society* **1992**, *114*, 10834-10843; b) C. Kresge, M. Leonowicz, W. Roth, J. Vartuli, J. Beck, *Nature* **1992**, *359*, 710-712.

[22] a) J. Chen, Y. Li, L. Huang, C. Li, G. Shi, *Carbon* **2015**, *81*, 826-834; b) J. Chen, B. Yao, C. Li, G. Shi, *Carbon* **2013**, *64*, 225-229.

[23] K. M. Parida, D. Rath, *Journal of Molecular Catalysis A: Chemical* **2009**, *310*, 93-100.

[24] J. Coates, in: R.A. Meyers, Ed., *Encyclopedia of Analytical Chemistry,* John Wiley & Sons Ltd., Chichester, **2000,** 10881-10882.

[25] a) T. L. Barr, M. Yin, S. Varma, *Journal of Vacuum Science & Technology A: Vacuum, Surfaces, and Films* **1992**, *10*, 2383-2390; b) P. Lihitkar, S. Violet, M. Shirolkar, J. Singh, O. Srivastava, R. Naik, S. Kulkarni, *Materials Chemistry and Physics* **2012**, *133*, 850-856.

[26] a) B. R. Strohmeier, D. M. Hercules, *Journal of Catalysis* **1984**, *86*, 266-279; b) L. Dake, D. Baer, J. Zachara, *Surface and Interface Analysis* **1989**, *14*, 71-75.

[27] S. A. Schmidt, N. Kumar, A. Shchukarev, K. Eränen, J.-P. Mikkola, D. Y. Murzin, T. Salmi, *Applied Catalysis A: General* **2013**, *468*, 120-134.

[28] H. Yan, X. Tao, Z. Yang, K. Li, H. Yang, A. Li, R. Cheng, *Journal of Hazardous Materials* **2014**, *268*, 191-198.

[29] a) T. Qiang, Y. Song, J. Zhao, J. Li, *Journal of Alloys and Compounds* **2019**, *770*, 792-802; b) E. C. Santos, L. S. Costa, E. S. Oliveira, R. A. Bessa, A. D. Freitas, C. P. Oliveira, R. F. Nascimento, A. R. Loiola, *Journal of the Brazilian Chemical Society* **2018**, *29*, 2378-2386; c) S. El-Hakam, A. I. Ahmed, E. Abdel-Galil, S. M. EL-Dafrawy, A. Al-Khamri, *Research Journal of Pharmaceutical Biological and Chemical Sciences* **2017**, *8*, 2604-2622.

[30] H. Shi, W. Li, L. Zhong, C. Xu, *Industrial & Engineering Chemistry Research* **2014**, *53*, 1108-1118.

[31] P. Fei, M. Zhong, Z. Lei, B. Su, *Materials Letters* **2013**, *108*, 72-74.

[32] D. Kharismadewi, Y. Haldorai, V. H. Nguyen, D. Tuma, J.-J. Shim, *Composite Interfaces* **2016**, *23*, 719-739.

[33] C. Li, M. She, X. She, J. Dai, L. Kong, *Journal of Applied Polymer*

science **2014**, *131*.

[34] X. Liu, Y. Zhou, W. Nie, L. Song, P. Chen, *Journal of Materials Science* **2015**, *50*, 6113-6123.

[35] M.-Q. C. Le, X. T. Cao, W. K. Lee, S.-S. Hong, K. T. Lim, *Molecular Crystals and Liquid Crystals* **2017**, *644*, 160-167.

[36] Y. Ho, G. McKay, *Process Safety and Environmental Protection* **1998**, *76*, 332-340.

[37] a) W. Kaminski, E. Tomczak, P. Tosik, *Desalination and Water Treatment* **2016**, *57*, 22774-22778; b) Y.-S. Ho, G. McKay, *Process Biochemistry* **1999**, *34*, 451-465.

[38] M. Jian, C. Tang, M. Liu, *Journal of Dispersion Science and Technology* **2014**, *35*, 1468-1475.

[39] Y. Wu, H. Qi, C. Shi, R. Ma, S. Liu, Z. Huang, *RSC Advances* **2017**, *7*, 31549-31557.
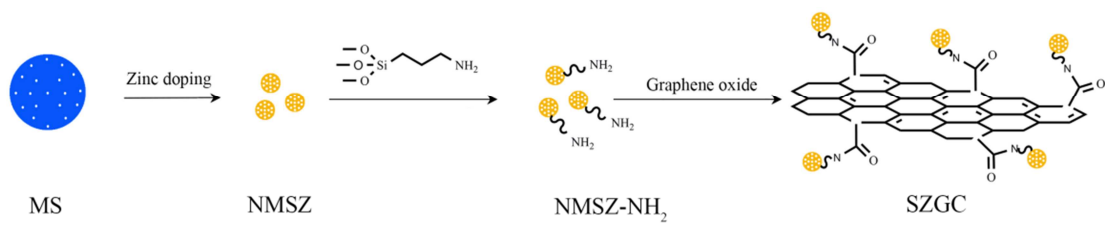
Fig.1. Synthesis of GO-NMSZ
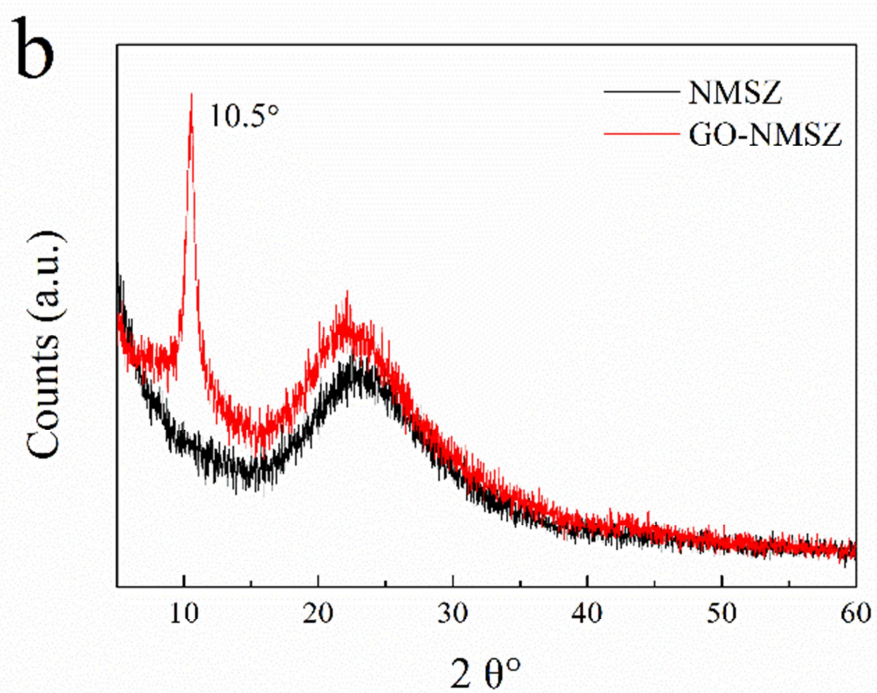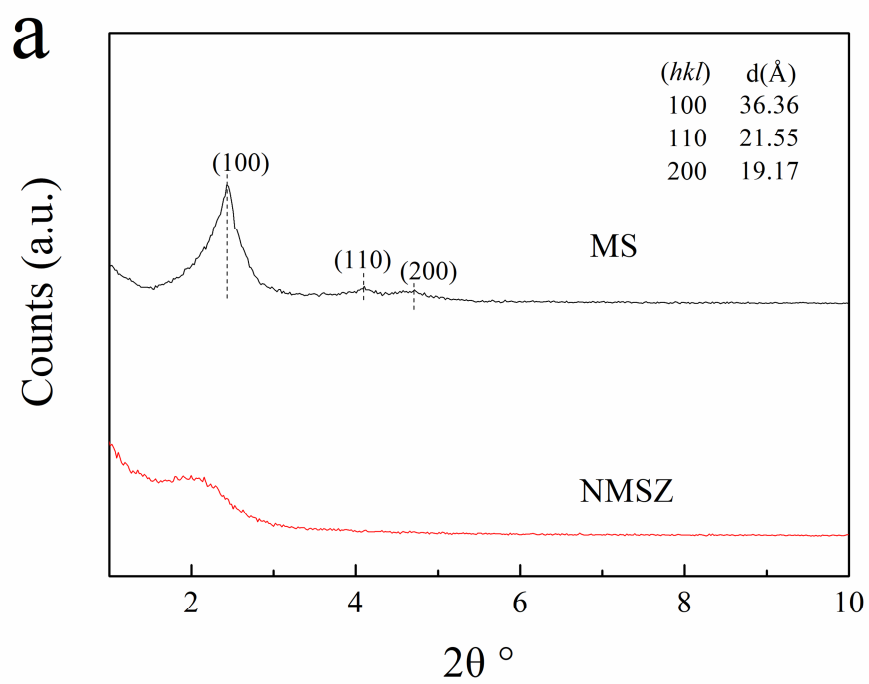
Fig. 2 (a) Small-angle XRD patterns of MS and NMSZ and (b) XRD patterns of NMSZ and GO-NMSZ.
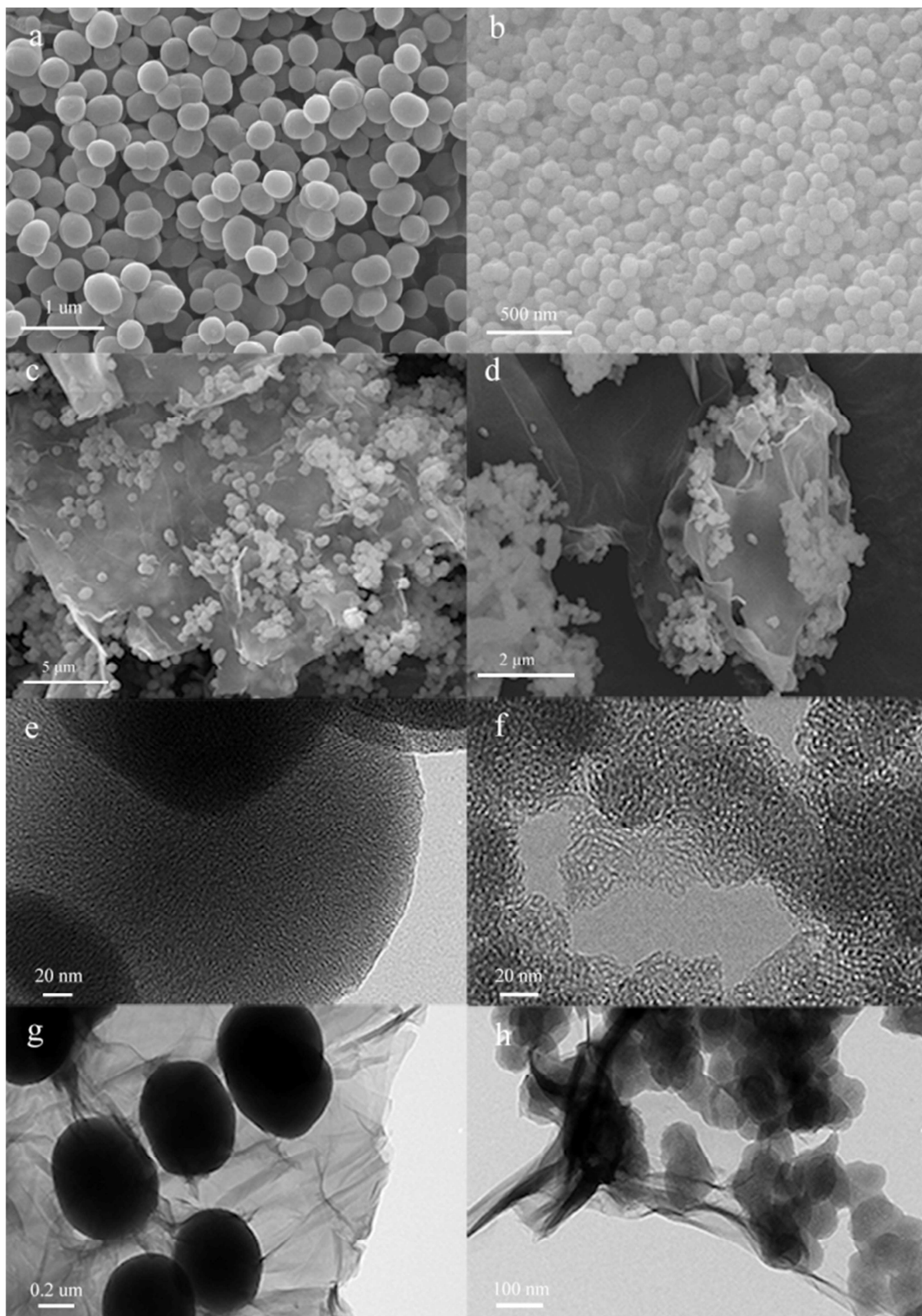
Fig. 3 (a to d) SEM and (e to h) TEM images of (a and e) MS, (b and f) NMSZ, (c and g) GO-MS and (d and h) GO-NMSZ.
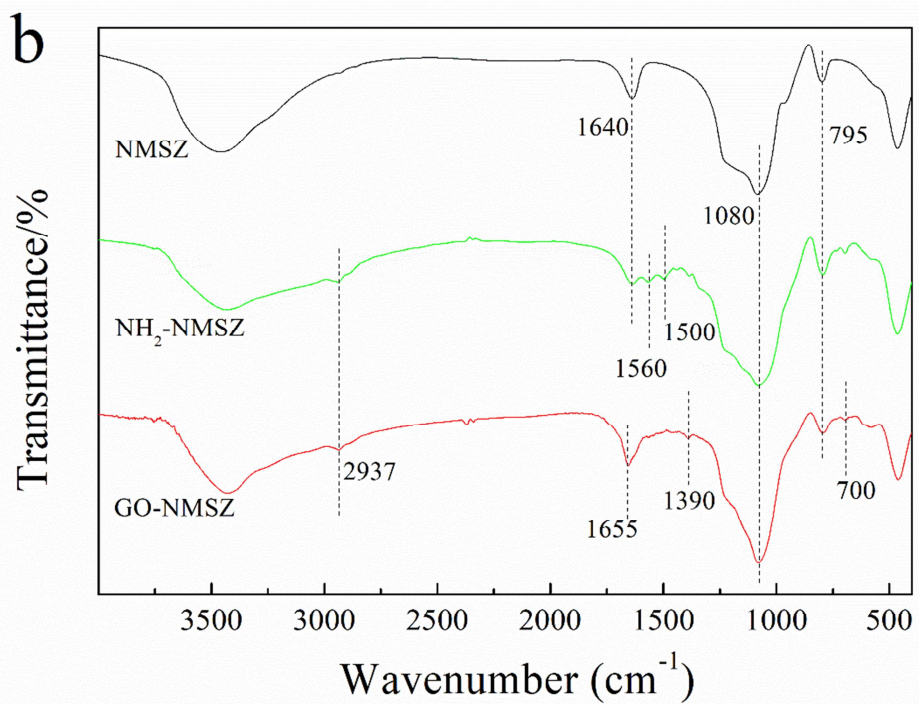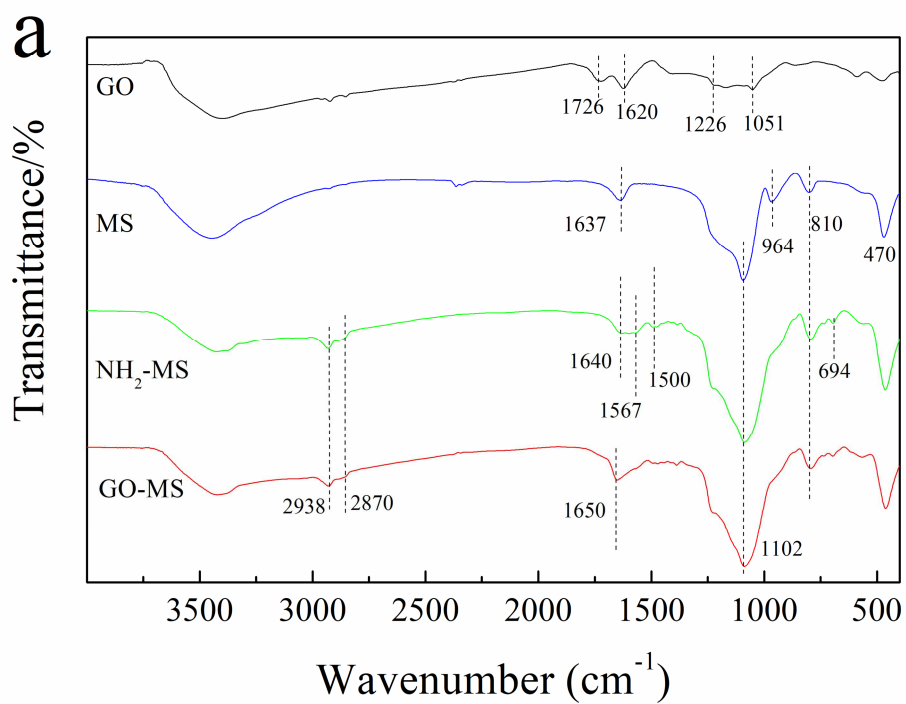
Fig. 4 FT-IR spectra of studied samples
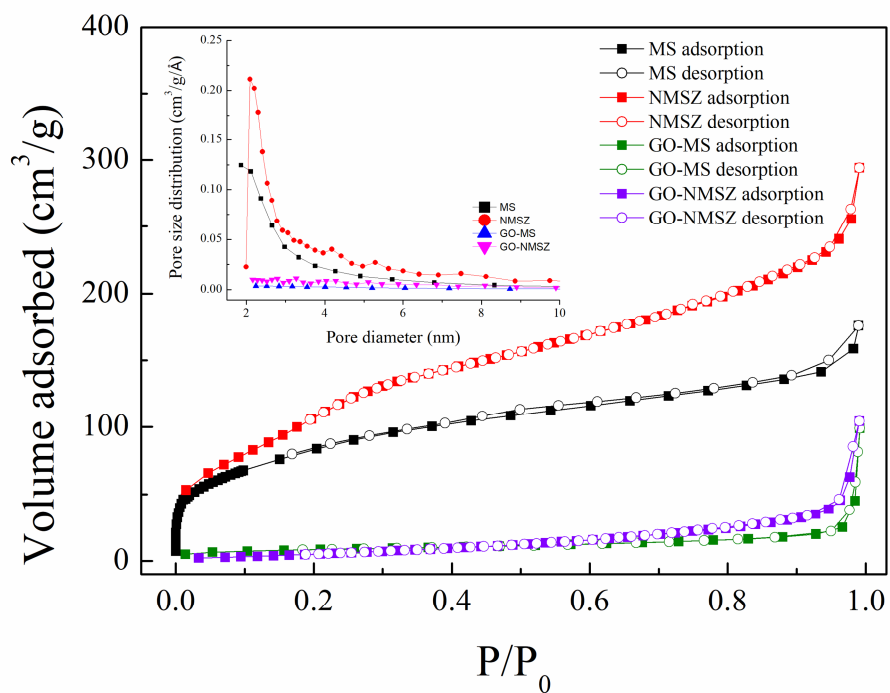
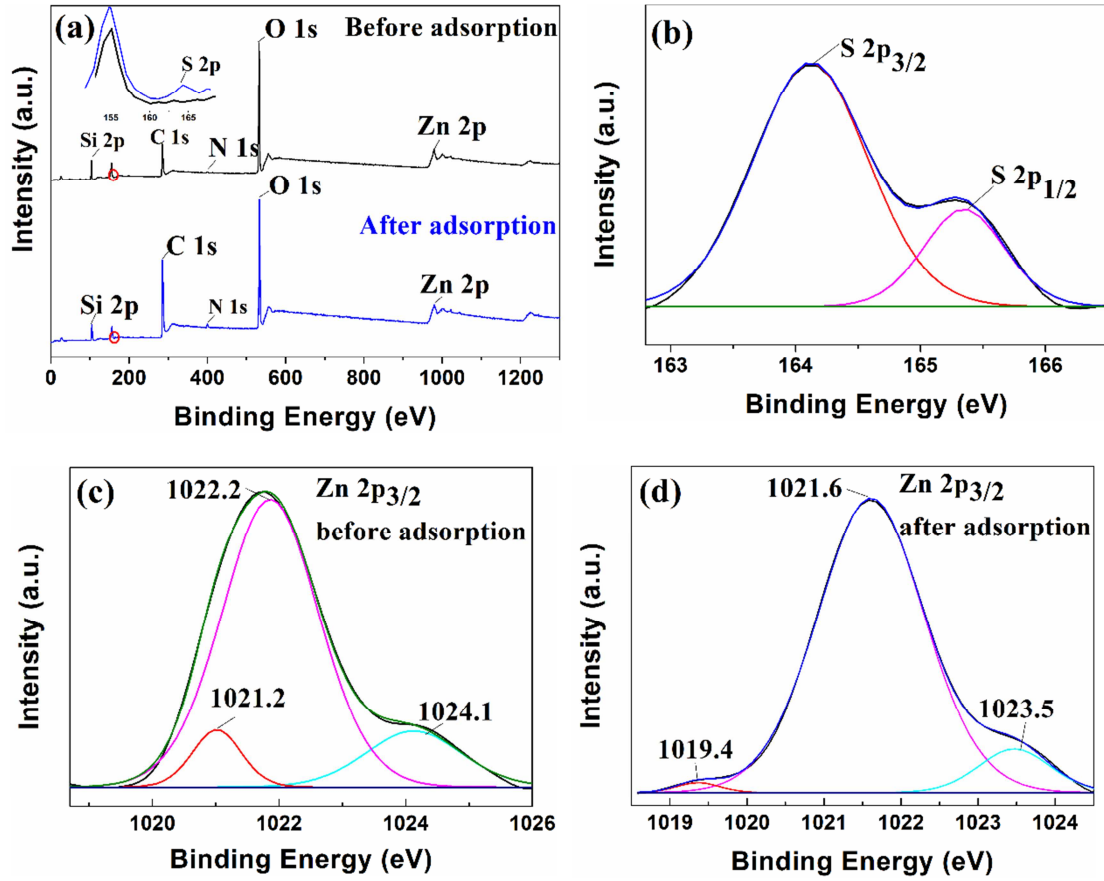Fig. 5 Nitrogen adsorption/desorption isotherms and corresponding pore-size distributions of studied samples

Fig.6 XPS spectra of (1) GO-NMSZ before and after adsorption (2) S 2p (3) Zn $2p_{3/2}$ before adsorption and (4) Zn $2p_{3/2}$ after adsorption
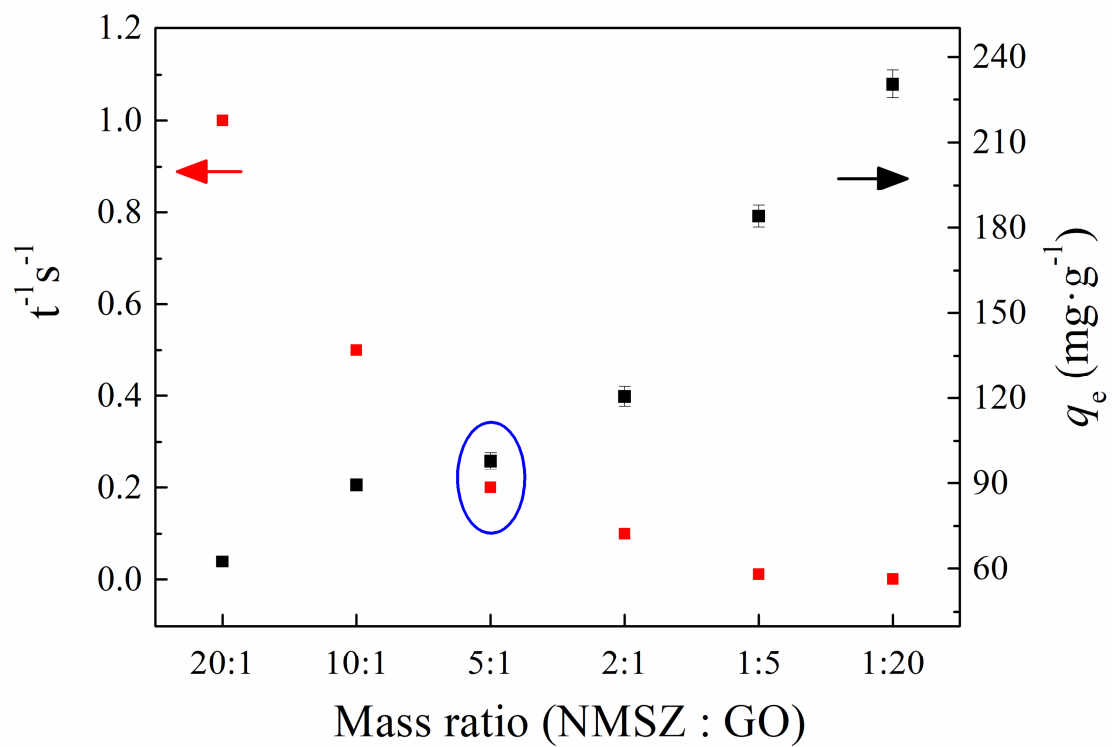
Fig. 7. The dependence of mass ratio on adsorption capacity and filtration efficiency in GO-NMSZ composites
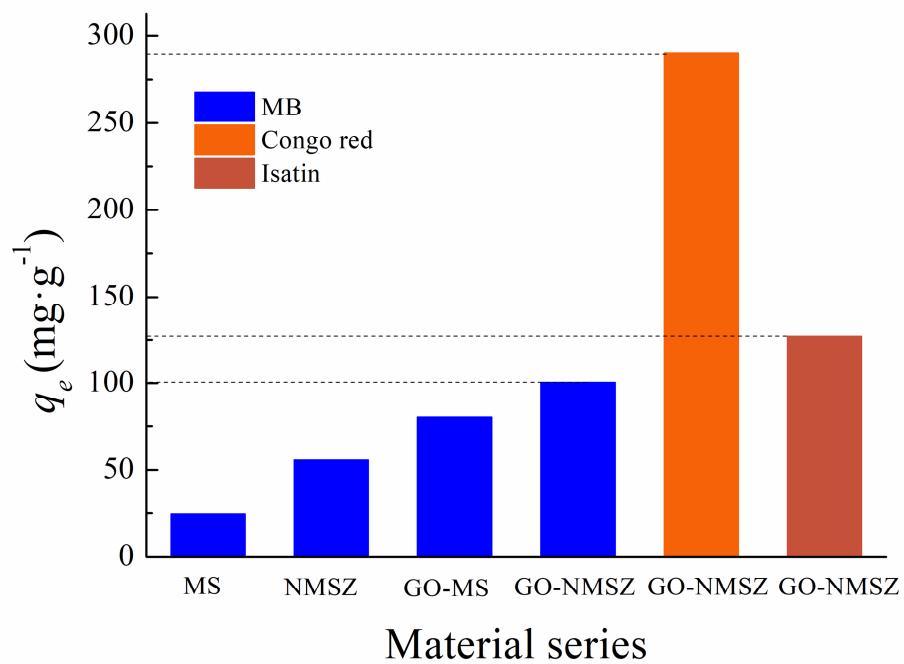
Fig.8 Adsorption capacity of MB onto studied samples (initial concentration = 200 mg·L^{-1}, pH = 6.5, temperature = 25 °C, mass ratio = 1 mg·mL^{-1})
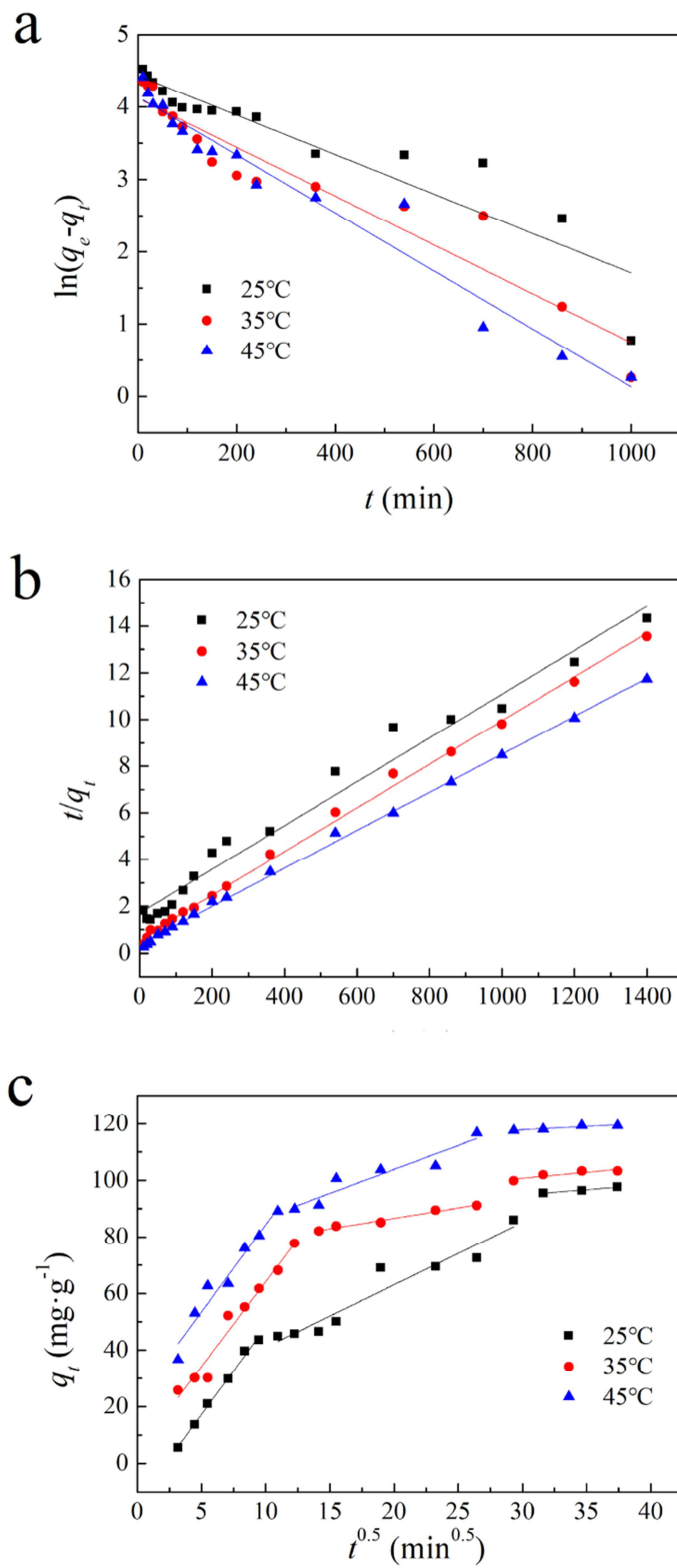
Fig. 9 Plots showing kinetics of MB removal by NMSZ at different temperatures, with fits using (a) pseudo-first-order model, (b) pseudo-second-order model and (c) Webber-Morris model.
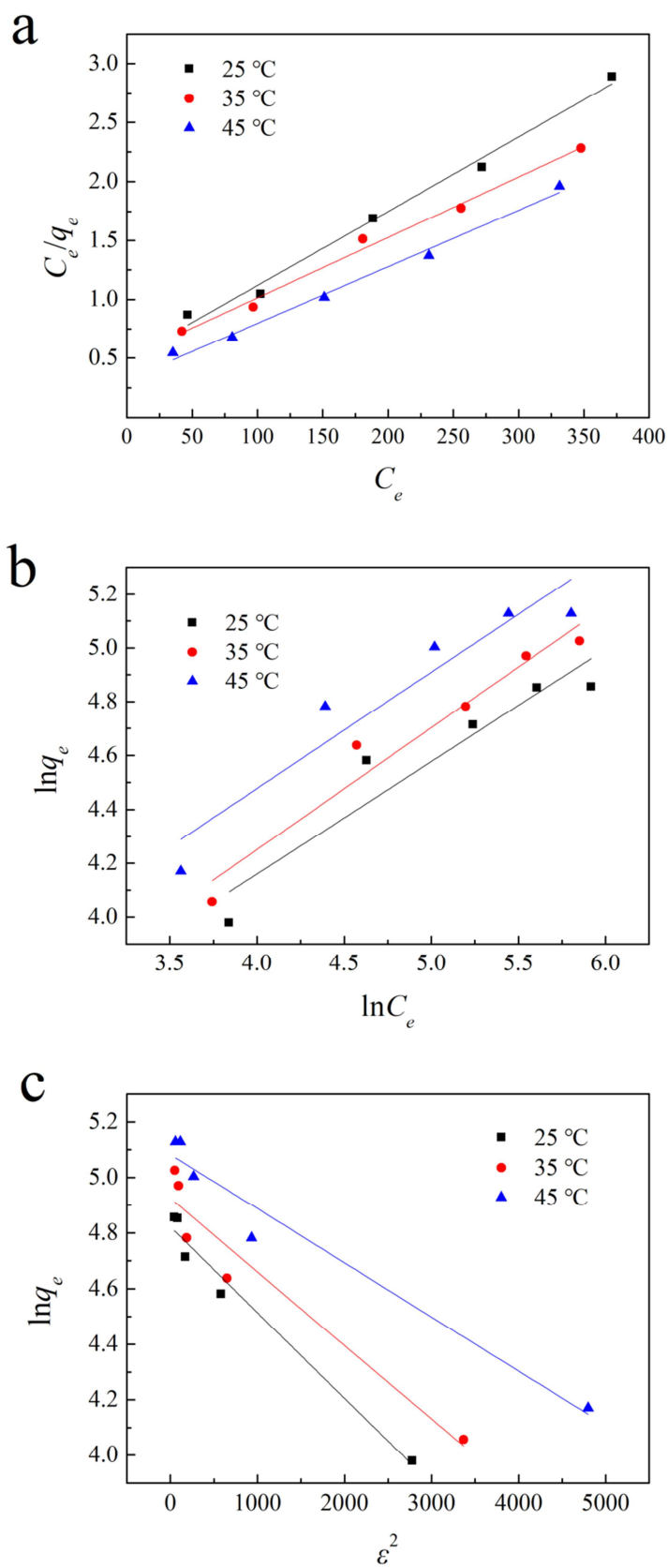
Fig. 10 Linearized isotherms for MB adsorption onto SZGC (a) Langmuir isotherm, (b) Freundlich isotherm and (c) Dubinin-Radushkevich isotherm.
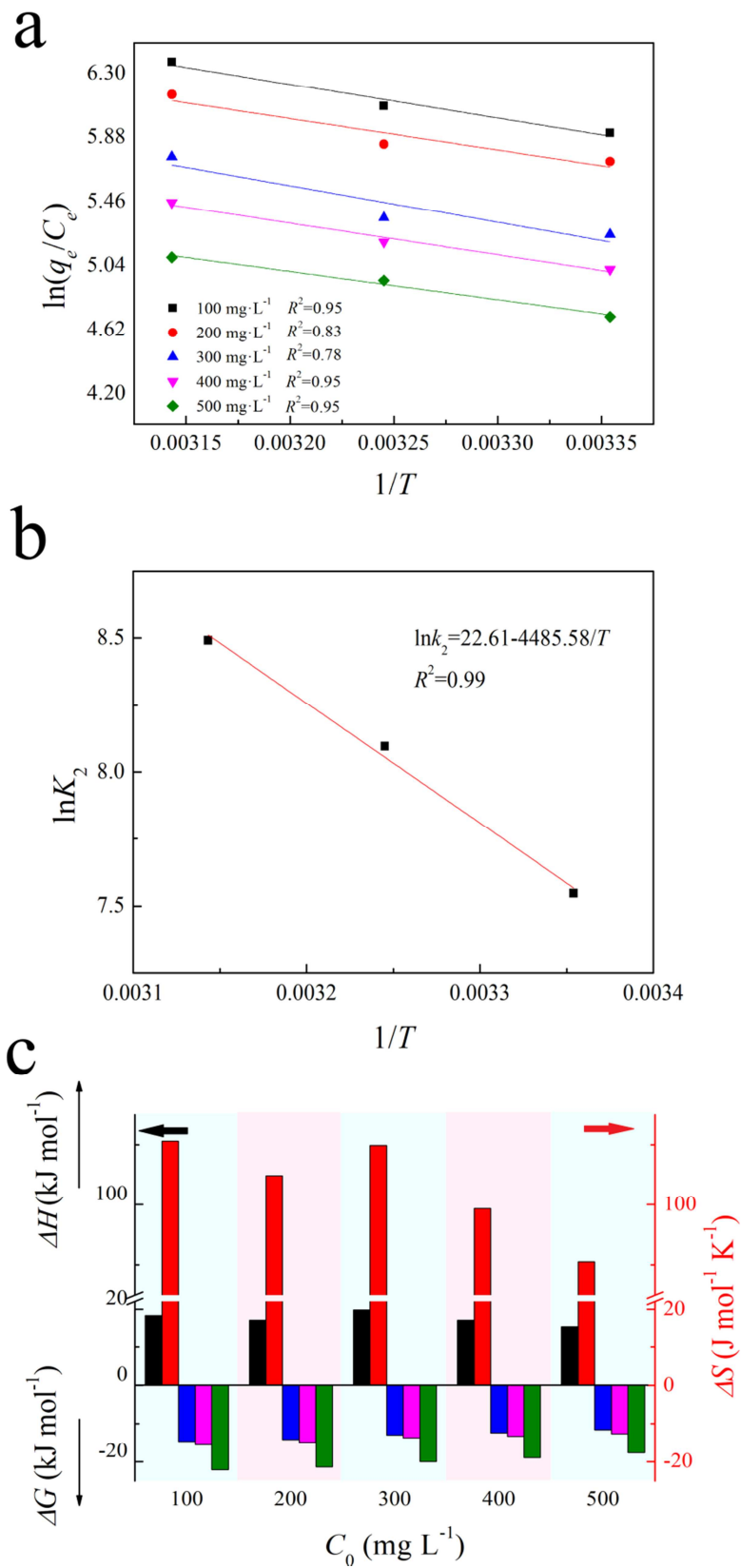
Fig. 11 Thermodynamic analysis (a) $\ln(q_e/C_e)$ versus $1/T$, (b) $\ln k_2$ versus $1/T$ and (c) thermodynamic parameters